China Welding 34 (2025) 100009

Contents lists available at ScienceDirect

China Welding

journal homepage: www.keaipublishing.com/en/journals/china-welding/

Wear performance and microstructures of Fe-Cr-C alloy cladding on heterogeneous welded joints of NM450/ER70-G/ZG30SiMn

Ning Xiao[a,b], Yujie Tao[c], Yiheng Liu[c], Haoyu Kong[c], Qingjie Sun[a], Ninshu Ma[b,*]

[a] METALLECO Inc, No. 3185 Dundas St W, 2F, Oakville, Ontario L6M 4J4, Canada
[b] Joining and Welding Research Institute, The University of Osaka, 11-1 Mihogaoka, Osaka 567-0047, Japan
[c] STUAA Automation Co., Ltd, No. 1000 South Langyatai Road, Qingdao 266400, China

A R T I C L E I N F O

Keywords:
Fe-Cr-C alloy cladding
NM450/ER70-G/ZG30SiMn heterogeneous joint
Dilution ratio
Microstructural characteristics
Wear performance

A B S T R A C T

This work employed Fe-Cr-C alloy as the cladding material to fabricate wear-resistant coatings on dissimilar steel welded joints composed of NM450 wear-resistant steel and ZG30SiMn cast steel with ER70-G welding wire. The investigation focused on elucidating the effect of dilution ratio levels on microstructural distribution and wear behavior within this heterogeneous multi-material system. Owing to its inherently higher chromium (Cr) content, the NM450 region demonstrated more pronounced carbide formation compared to the ER70-G and ZG30SiMn regions. Microstructural analysis revealed that Cr_7C_3 carbides predominantly formed along grain boundaries, whereas $Cr_{23}C_6$ carbides mainly precipitated within grains. After cladding, the wear resistance of the NM450/ER70-G/ZG30SiMn welded joint was markedly improved, with the high-dilution coating exhibiting superior performance. This enhancement was attributed to favorable thermal conditions in the high-dilution scenario, promoting a more homogeneous precipitation of $Cr_{23}C_6$. Although significant elemental mixing occurred at the interfacial zones, the top region of the cladding layer remained minimally affected by dilution-induced drawbacks. Accordingly, the high-dilution sample demonstrated better wear resistance than its low-dilution counterpart due to optimized carbide precipitation characteristics. These findings provide basic insights for designing effective cladding strategies for complex multi-material components in demanding industrial applications.

1. Introduction

In the field of engineering, surface friction damage represents one of the most prevalent failure modes. Replacing entire damaged components not only escalates economic costs but also prolongs production cycles. Consequently, implementing localized repairs on affected surfaces or applying a preemptive wear-resistant coating prior to formal production can significantly mitigate failure risks while enhancing operational efficiency. This approach offers substantial advantages in terms of both cost-effectiveness and process optimization, making it a strategically valuable solution for industrial applications [1,2].

Conventional surface treatment approaches typically employ welding technologies to fabricate cladding layers on target surfaces. Aslam et al. [3] successfully deposited a 304 stainless steel coating on mild steel using tungsten inert gas (TIG) welding, leveraging the alloy's high chromium (Cr, 18–20 wt.%) and nickel (Ni, 8–10 wt.%) content to enhance surface hardness from 177 HV0.5 to 335 HV0.5, while simultaneously reducing the average wear depth from 146 μm to 57 μm. In a comparable study, Wang et al. [4] applied Fe105 powder containing approximately 17 wt.% Cr onto QT500-7 ductile iron substrates. Through optimized processing parameters, they achieved crack-free deposition with a 30 % dilution ratio, resulting in a remarkable 103 % improvement in surface hardness from 208.5 $HV_{0.2}$ to 424.2 $HV_{0.2}$. Zhang et al. [5] utilized an Fe-based powder containing 6.2 wt.% Cr and 6.3 wt.% V as wear-resistant material, achieving an exceptional surface hardness of 823.6 $HV_{0.025}$ — representing a 3.9-time increase over the base material hardness. This treatment also produced a dramatic two-order-of-magnitude reduction in wear rate, decreasing from 1.03×10^{-6} mm^3/(N m) to 2.22×10^{-8} mm^3/(N m).

The aforementioned methods primarily focus on enhancing hardness through selecting appropriate cladding materials to mitigate surface damage. Liu et al. [6] have demonstrated that post-treatment

Peer review under the responsibility of Editorial Board of China Welding.

* Corresponding author.
E-mail address: ma.ninshu.jwri@osaka-u.ac.jp (N. Ma).

https://doi.org/10.1016/j.cwe.2025.100009
Received 8 June 2025; Received in revised form 25 September 2025; Accepted 28 September 2025
Available online 13 November 2025

processes can further optimize wear resistance. They employed a low-temperature plasma nitriding process to post-treat AISI 316L cladding layers, achieving remarkable improvements in both surface hardness and wear performance. Their results showed that the nitriding treatment not only reduced the friction coefficient but also decreased the wear rate from 2.31×10^{-5} $mm^3/(N\ m)$ to 1.61×10^{-7} $mm^3/(N\ m)$. More significantly, the treatment induced a transformation in the dominant wear mechanism from abrasive and adhesive wear to oxidative and adhesive wear. Moreover, advanced modification of cladding material composition through the incorporation of non-metallic elements such as boron (B) can significantly enhance wear resistance by promoting the formation of additional hard phases within the cladding layer. Santana et al. [7] demonstrated this approach by employing B-enhanced Fe-based powder as cladding material on mild steel substrates. Their microstructural analysis revealed an α-(Fe, Cr) solid solution matrix containing numerous micron- and nano-scale (Fe, Cr)NbB and M2B (M = Cr, Fe) boride precipitates, which collectively improved the wear resistance of the mild steel substrate by approximately tenfold. Further studies have shown that B addition to Fe-Cr-C alloys not only facilitated the formation of various boride phases (Fe2B, CrB2, Fe23B6, Cr5B3) [8], thereby increasing both the variety and quantity of hard phases, but also promoted the nucleation of primary Cr7C3 carbides while refining their grain size. This dual effect enabled the achievement of cladding layer hardness exceeding 1000 HV10 [9,10]. However, it should be noted that excessive formation of these borides and carbides may lead to their network-like distribution within the matrix. While such microstructure demonstrated excellent wear resistance under relatively low loads (< 20 N), it became problematic under higher stress conditions (> 25 N) where these hard phases may act as stress concentration sites and initiate crack formation [11]. This phenomenon highlights the importance of optimizing hard phase content and distribution to balance wear resistance and mechanical integrity under varying service conditions, presenting a critical consideration for the design of advanced wear-resistant coatings in practical engineering applications.

Recent studies have revealed that the incorporation of nanoscale TiC particles produces multifaceted improvements in cladding layer performance. Beyond promoting equiaxed grain formation and microstructure refinement, these ceramic additions simultaneously enhanced hardness and Young's modulus, thereby improving both resistance to plastic deformation and elastic recovery capability [12–14]. Despite under severe loading conditions (100 N), TiC-reinforced coatings demonstrated a 5.4-time increase in hardness over the Q345C substrate [15], a 50 % reduction in friction coefficient and a 40 % decrease in mass loss compared to unreinforced counterparts [16]. Reinforcement with SiC particles induced formation of additional intermetallic phases including CrSi2 and Mn3Ni2Si alongside conventional carbides (Fe2C, Fe5C2, Cr7C3), resulting in remarkable 8.7-fold and 1.7-fold improvements in adhesive wear resistance and abrasive wear resistance for mild steel base materials, respectively [17]. WC particle addition similarly functioned as effective heterogeneous nucleation sites, facilitating columnar-to-equiaxed transition and grain refinement. While optimal WC content (30 wt.%) enhanced both impact resistance and sliding wear resistance, excessive addition (>40 wt.%) tended to induce crack initiation due to increased brittleness [18,19].

The research findings reveal important trade-offs in wear-resistant coating design. While alloying elements and ceramic particles can effectively increase hard phase content, these inherently brittle compounds may cause interfacial mismatch and crack initiation when present in excessive quantities [20]. Furthermore, the powder-based alloy modification approach, despite its compositional flexibility, faces inherent limitations including poor coating density, porosity formation [21,22], and particle agglomeration/flotation issues that compromise microstructural homogeneity [16]. In contrast, wire-based Fe-Cr-C cladding offers distinct advantages through its simpler processing, higher coating density, and cost-effectiveness—factors that have made this system particularly attractive for industrial applications [23]. The wear resistance of Fe-Cr-C coatings primarily stems from M7C3 and M23C6 carbides (where M represents Cr and Fe), with their relative proportions being strongly composition-dependent. At lower carbon concentrations (1–3 wt.%), M23C6 predominates, while higher carbon levels (5–6 wt.%) favor M7C3 formation [24,25]. Cr content plays a dual role: while it promotes carbide formation, excessive Cr (≥25 wt.%) leads to coarse primary carbides with reduced toughness that paradoxically diminish wear resistance [26]. The study by [27] further highlights that the high contents of Cr and C can trigger excessive hard phase formation, generating internal stresses that promote cracking and weaken coating-substrate bonding. These findings underscore the importance of balanced alloy design in Fe-Cr-C systems, where optimal wear performance requires careful control of both carbide volume fraction and morphology to achieve the desired combination of hardness and fracture resistance.

While existing research has predominantly focused on enhancing wear resistance in homogeneous materials, practical engineering components often consist of multiple material systems. A representative example is the scraper conveyor in mining applications, where the load-bearing structure typically comprises cast steel while the working components employ wear-resistant steel. The interface between these dissimilar materials frequently experiences severe chain-induced abrasion, leading to inevitable surface degradation. This highlights a critical research gap in addressing wear behavior at heterogeneous material junctions. The present study investigates this underexplored area by employing ZG30SiMn/NM450 dissimilar steel joints as base materials and Fe-Cr-C alloy as cladding material. This experimental approach aims to elucidate wear resistance distribution patterns in multi-material systems, with particular focus on the interfacial transition zone between dissimilar steels. The research objectives include characterizing dilution ratio level and microstructure evolution across material boundaries, evaluating hardness gradients and their correlation with wear performance. This work seeks to establish fundamental principles for wear resistance control in complex multi-material components. The findings are expected to provide valuable insights for surface engineering of critical industrial equipment where dissimilar material joining is unavoidable.

2. Materials and methods

2.1. Cladding experiment setup

The substrate material for the arc cladding experiment was a narrow-gap welded joint (NM450/ZG30SiMn dissimilar steel joint filled with ER70-G weld metal (WM)). Both the NM450 and ZG30SiMn base metals (BMs) were 400 mm in length, 100 mm in width, and 40 mm in thickness; whereas the width of the rectangular narrow-gap groove was 12 mm. The NM450/ER70-G/ZG30SiMn dissimilar steel narrow-gap welded joint was prepared by gas metal arc welding (GMAW). A KB968 solid wire with a diameter of 1.2 mm was employed as the cladding filler material, the chemical compositions of which are listed in Table 1. The KB968 wire contains moderate levels of Cr and C, ensuring sufficient formation of Cr-C wear-resistant phases while preventing excessive hard phases that could induce cracking in the cladding layer.

The gas metal arc cladding experiments were carried out by a FANUC industrial robot that was fitted with a MEGMEET melted

Table 1
Chemical compositions of cladding materials (wt.%).

Materials	Cr	Nb	Si	Mn	C	Fe
ZG30SiMn	0.43	—	0.64	1.39	0.28	Bal.
NM450	0.86	—	0.35	1.61	0.21	Bal.
ER70-G	0.30	—	0.30	1.45	0.10	Bal.
KB968	13.5	7.00	1.50	2.00	3.50	Bal.

Table 2
Detailed cladding parameters.

No.	Average welding current/A	Peak welding current/A	Base welding current/A	Pulse frequency/Hz	Arc voltage/V	Deposition speed/(mm·min^{-1})	Wire feed speed/(mm·min^{-1})
1	180	197	75	140	29	400	9
2	240	254	126	140	33	400	12

electrode welding machine. Before cladding, the surface of the dissimilar steel welded joint was mechanically polished by an angle grinder to remove impurities and ensure a consistent surface flatness, and then further cleaned by absolute ethyl alcohol. Single-layer multi-pass cladding experiments were conducted under various currents, with detailed process parameters provided in Table 2. During cladding, a unidirectional travel path (from ZG30SiMn to NM450, as illustrated in Fig. 1a) was maintained, with a constant overlap ratio of 20 % and an inter-pass cooling time of 5 min. The wire stick-out length was set to 17 mm, and pure CO_2 shielding gas was supplied at a flow rate of 20 L/min.

2.2. Material characterization

After the cladding experiments, metallographic specimens were extracted from both the longitudinal and transverse cross-sections of the cladding layer using wire electrical discharge machining to observe the macrostructures and microstructures. The sampling orientations are schematically illustrated in Fig. 1a. The specimens were ground by 80#–2000# sandpapers, followed by diamond polishing paste with a diameter of 2.5 μm, finally etched with $FeCl_3$ + HCl + H_2O reagent ($FeCl_3$: 5 g, HCl: 50 mL, and H_2O: 100 mL) for 15 s to reveal the microstructure, which was subsequently examined using optical microscopy (OM, OLYMPUS DSX510).

Due to the dissimilar steel welded joint (NM450/ER70-G/ZG30SiMn), the cladding layer formed three distinct heterogeneous interfaces: NM450/cladding layer, ER70-G/cladding layer, and ZG30SiMn/cladding layer. Additionally, two compositional mixing zones were observed: NM450/ER70-G/cladding layer and ER70-G/ZG30SiMn/cladding layer. Microhardness testing (Vickers hardness tester, HVS-1000) and X-ray diffraction (XRD, DX-2700) analysis were performed on the three interfaces. The hardness measurements were conducted under a 200 g load for 15 s, with a 0.2 mm spacing between indentations. XRD scans were performed over a 2θ range of 20°–100° at a scanning rate of 2°/min. Furthermore, scanning electron microscopy (SEM, MERLIN COMPACT) equipped with energy dispersive spectroscopy (EDS) was employed to analyze the phase composition across all three interfaces and two mixing zones. The sampling strategy for material characterization is depicted in Fig. 1c, while the methodology for calculating the cladding layer dilution ratio (δ) is illustrated in Fig. 1d.

2.3. Wear resistance evaluation

To ensure accurate evaluation of the wear resistance performance of the cladding layers, specimens were sampled from the cladding layers of three distinct zones (NM450, ER70-G, and ZG30SiMn). Concurrently, wear resistance tests were conducted on their corresponding base materials (NM450, ER70-G, and ZG30SiMn), as depicted in Fig. 1b. The wear test specimens were machined to dimensions of 5 mm in thickness and 15 mm in diameter. Wear testing was conducted under a 10 N normal load using GCr15 steel as the counter face material, with a rotational speed of 500 r/min per minute and a wear track radius of 5 mm. The wear resistance was comprehensively evaluated through: friction coefficient calculation, weight loss measurement, and worn surface morphology analysis (via SEM microscopic examination).

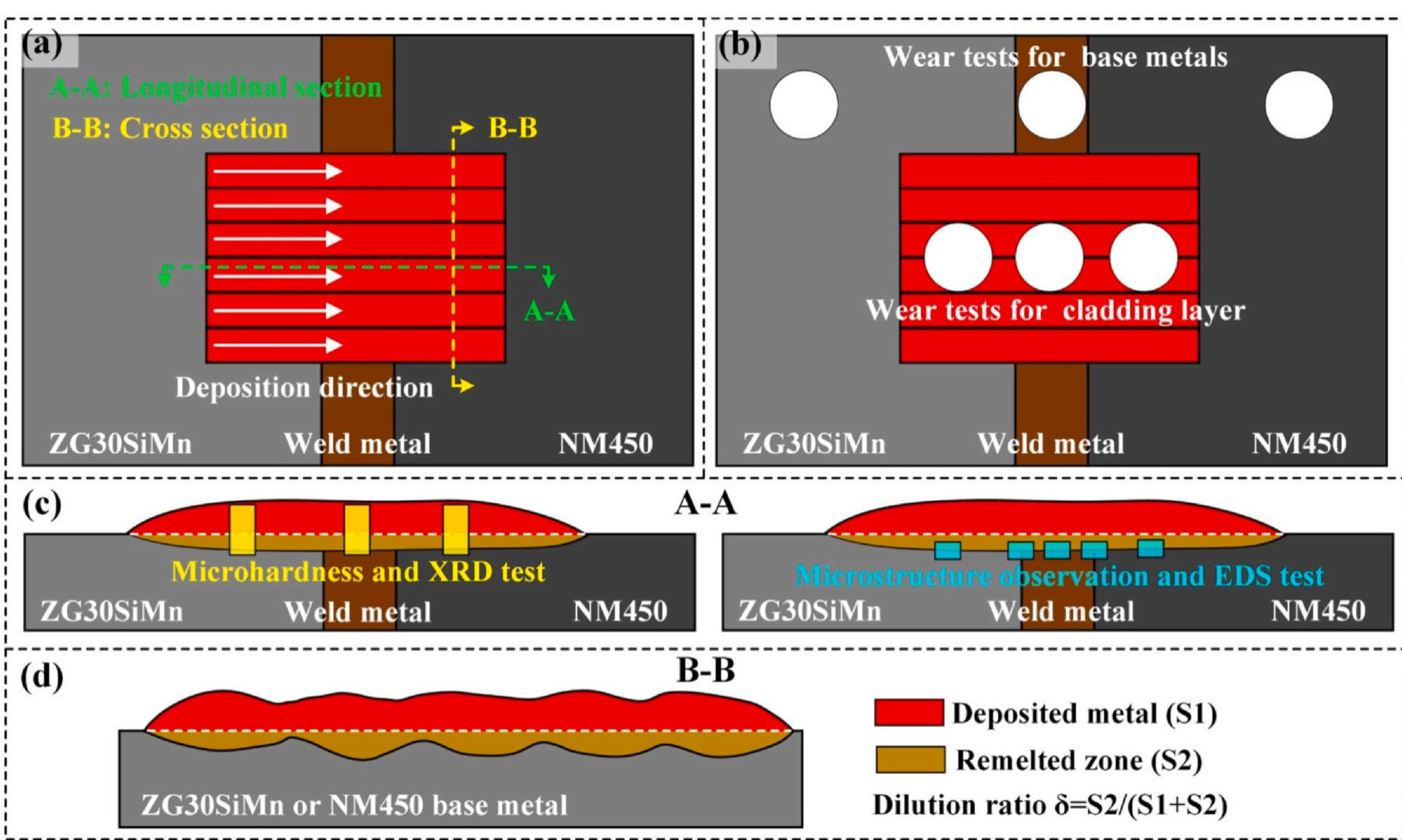

Fig. 1. Schematic illustration of the cladding process: (a) Deposition strategy, (b, c) Wear test and material characterization sampling methodology, (d) Dilution ratio calculation approach.

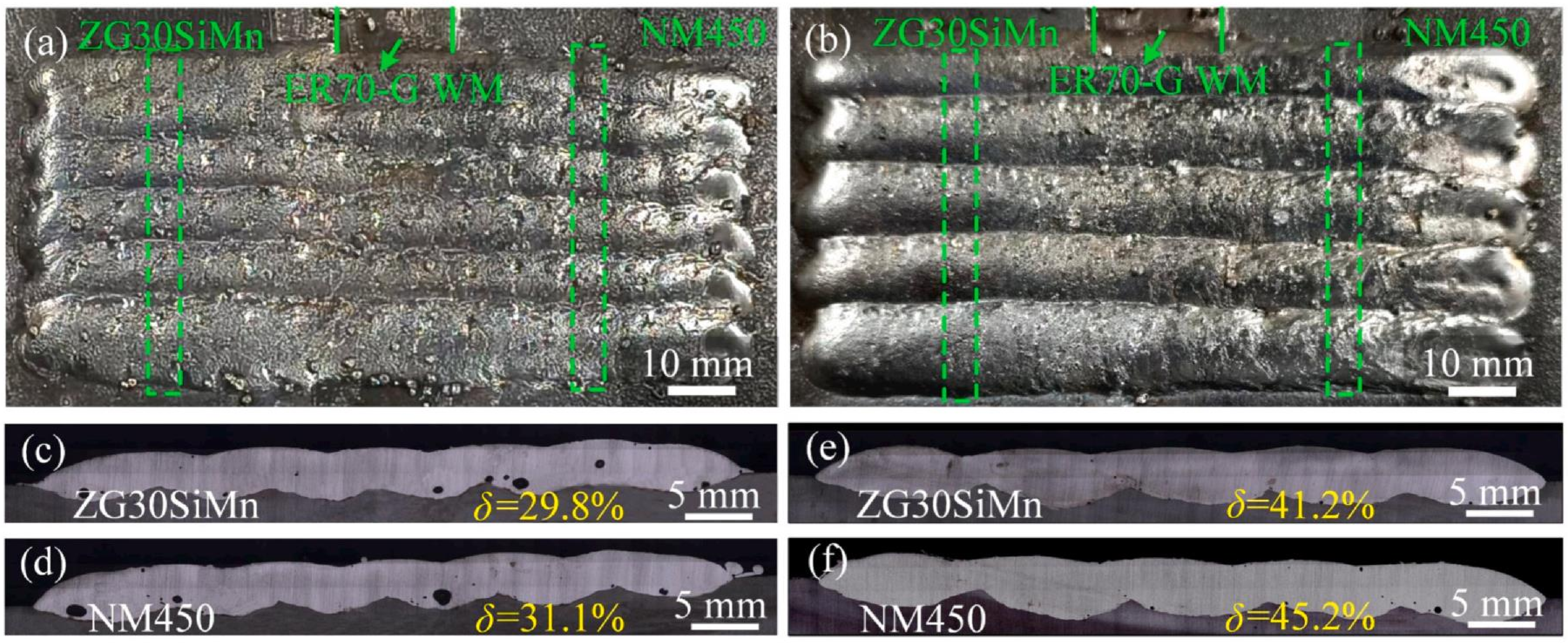

Fig. 2. Macro-morphology of the cladding layer: (a) General macro-morphology at parameters of group 1, (b) general macro-morphology at parameters of group 2, (c, d) Cross-sectional morphologies of the ZG30SiMn and NM450 regions at low dilution ratios, (e, f) Cross-sectional morphologies of the ZG30SiMn and NM450 regions at high dilution ratios.

3. Results and discussion

3.1. Macro-morphology

Fig. 2a, b presents the macroscopic morphology of cladding layers deposited under different cladding parameters. All cladding conditions produced straight, continuous layers without visible cracks, confirming the suitability of the selected KB968 wire. Due to the narrow width of the ER70-G WM and the predominant base materials (ZG30SiMn and NM450), cross-sectional analysis focused on the ZG30SiMn and NM450 regions, with sampling locations marked by green dashed rectangles in Fig. 2a, b. Cladding layer thickness was measured at three random locations to minimize statistical error. At lower currents, the average thickness measured 2.33 ± 0.18 mm of the ZG30SiMn region and 2.42 ± 0.24 mm of the NM450 region, while at higher currents the corresponding values were 2.30 ± 0.19 mm and 2.21 ± 0.08 mm, respectively. The thickness variation between regions of the same cladding layer remained within 5 %, demonstrating good surface uniformity. Notably, despite higher heat input and faster wire feed rate, no significant increase in cladding thickness was observed. Instead, a slight decrease occurred compared to the lower-current condition. This phenomenon suggests that increased heat input enhanced base material remelting, resulting in a larger remelting zone. The enhanced remelting effect directly influenced compositional mixing between the cladding layer and base material. Therefore, the dilution ratio was subsequently measured. At lower currents, the dilution ratios of the ZG30SiMn and NM450 regions were 29.8 % and 31.1 %, respectively, while at higher currents, these values increased to 41.2 % and 45.2 %, indicating greater dilution ratio with higher heat input. Additionally, porosity was observed to decrease at higher heat input, likely due to prolonged molten pool duration facilitating more effective gas escape. The varied dilution ratio under different cladding parameters indicated distinct elemental diffusion and interfacial mixing behaviors, suggesting corresponding microstructural modifications that warrant further investigation.

3.2. Metallographic observation

Fig. 3 presents the longitudinal section analysis of the low-dilution-ratio cladding layer, revealing microstructural characteristics across three heterogeneous interfaces: NM450/cladding, ER70-G/cladding, and ZG30SiMn/cladding. Metallographic examination demonstrates excellent interfacial bonding without cracking at all interfaces, confirming good compatibility between the selected wire and base materials. The microstructural evolution along the build direction shows a clear transition from prominent columnar grains in the bottom region to equiaxed grains in the middle and top sections. This gradient structure results from varying thermal conditions: the bottom region, being farthest from the heat source with optimal heat dissipation, experiences the highest thermal gradient, favoring columnar growth. Notably, white precipitates were observed to be non-uniformly distributed across all three interfaces, with apparently higher density in the NM450 region. Comparative analysis with Sousa et al.'s work on Fe-22Cr-5.5C alloy deposition (where similar precipitates were identified as M7C3 carbides) suggests these are likely carbide phases [28]. The observed variation in precipitate density may result from NM450′s higher Cr content (approximately 0.8 wt.%) compared to ZG30SiMn and ER70-G (typically < 0.5 wt.% Cr), which would enhance carbide formation during solidification.

Fig. 4 shows the longitudinal section analysis of the high-dilution-ratio cladding layer, revealing crack-free interfaces with all three base materials (NM450, ER70-G, and ZG30SiMn). The prolonged molten pool duration (attributed to higher heat input) in this condition reduced the thermal gradient, resulting in weaker columnar crystal characteristics at the cladding layer bottom compared to the low-dilution sample. Microstructural examination showed significantly more numerous and uniformly distributed white carbide precipitates throughout the NM450, ER70-G, and ZG30SiMn regions. However, a distinct vertical gradient in carbide precipitation was observed, with precipitate density increasing progressively from bottom to top. This distribution pattern directly correlates with the thermal history during cladding. The top zone, benefiting from direct arc heating and final solidification, maintained optimal conditions for carbide nucleation, while the bottom region's relatively rapid cooling limited carbide growth. Furthermore, the intense elemental mixing in the bottom region of the cladding layer—a consequence of high dilution ratio—led to substantially reduced Cr concentration, thereby substantially inhibiting carbide formation in this zone.

To determine the fundamental phase composition of the cladding layer, XRD analysis was conducted on the three distinct regions of the NM450, ER70-G, and ZG30SiMn. The XRD specimens, measuring 2.5 mm in length, were carefully prepared to encompass both the deposited zone and remelted zone while minimizing interference from the base materials. As shown in Fig. 5, the XRD patterns reveal that the cladding layer primarily consisted of an Fe matrix accompanied by various carbides including Fe_4C, Fe_3C, $Cr_{23}C_6$, Cr_3C_2, and Cr_7C_3. Comparative analysis demonstrates that the ER70-G region exhibited relatively fewer carbide peaks compared to the NM450 and ZG30SiMn

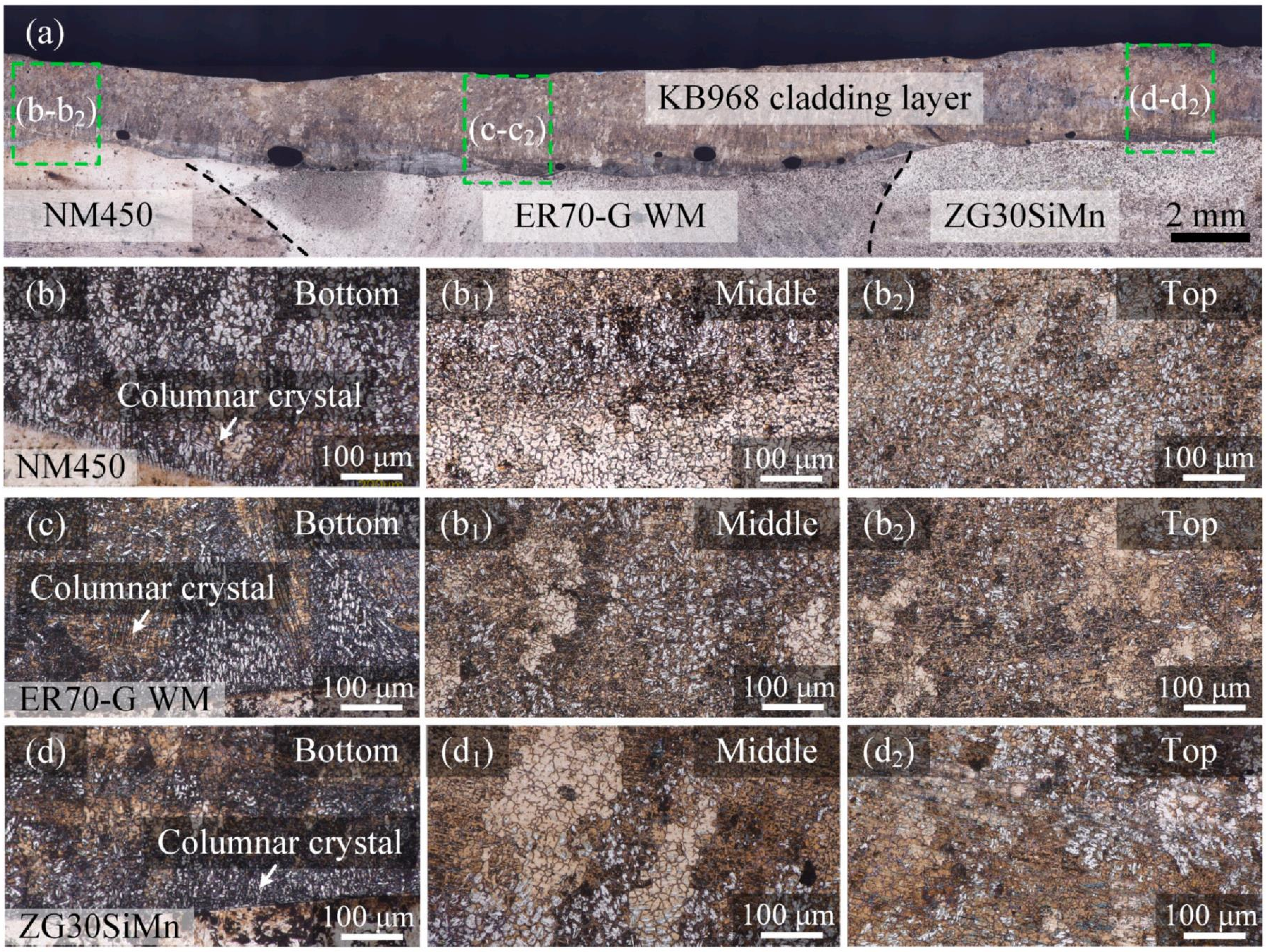

Fig. 3. Optical micrographs of the longitudinal section of the low-dilution-ratio cladding layer: (a) Macroscopic overview, (b–b_2) Across different height zones in the NM450 region (b: bottom, b_1: middle, b_2: top), (c–c_2) Corresponding zones in the ER70-G region, (d–d_2) Corresponding zones in the ZG30SiMn region.

regions, which can be attributed to its lower Cr content (as indicated in Table 1). While the variation in dilution ratio did not alter the fundamental phase species of the cladding layer, the high-dilution condition resulted in enhanced diffraction peak intensities of $Cr_{23}C_6$. This observation confirms the increased carbide precipitation previously observed via optical microscopy. The XRD result suggests that higher dilution ratio promoted more extensive carbide formation without changing the types of phases present.

Since the upper surface of the cladding layer, acting as the working surface, is directly subject to wear under external forces, we specifically observed the upper surface using an optical microscope, with the results shown in Fig. 6. Fig. 6a–c presents the morphologies of the upper surface of the cladding layer under low-dilution condition. When compared with the ER70-G and the ZG30SiMn regions, the NM450 region exhibited the largest number of carbides with the most uniform distribution. In contrast, the ER70-G and the ZG30SiMn regions showed extremely uneven carbide distribution, with a considerable portion showing almost no carbide precipitation. This indicates that the composition of base materials has a significant impact on the phase composition and wear resistance of the cladding layer—if the base material contains higher contents of elements such as Cr and C, it is more conducive to the precipitation and growth of carbides. While under high-dilution condition, the number of carbides increased significantly and their distribution uniformity was greatly improved, as shown in Fig. 6d–f. Furthermore, the upper surfaces of the NM450, ER70-G, and ZG30SiMn regions exhibited approximately similar carbide distribution morphologies. This phenomenon indicates that the growth tendency of carbides was enhanced under such conditions, and the discrepancy in carbide precipitate quantities caused by variations in base material composition was effectively reduced.

3.3. Microstructural distribution

While optical microscopy and XRD analysis can characterize the macroscopic structure of the cladding layer, a more detailed investigation is required to clarify the microstructural distribution characteristics of the heterogeneous interface under varying dilution ratios. Fig. 7 illustrates the microstructure of the NM450/cladding layer interface, with corresponding EDS results summarized in Table 3. A continuous white precipitated phase was observed along the grain boundaries, whereas two distinct contrasts—white and dark gray—- were evident inside the grains. EDS analysis revealed that the NM450 base material adjacent to the interface contained approximately 5.1 wt.% Cr, with the elevated Cr content primarily attributed to element mixing with the welding wire. Specifically, the dark gray intragranular phase exhibited a Cr content of 10.5 wt.%, while the white intragranular phase and white grain boundary phase contained 15.3 wt.% and 29.6 wt.% Cr, respectively. A clear correlation was observed between phase contrast and Cr content: white phases corresponded to higher Cr concentrations, with the grain boundary phase exhibiting the highest Cr content, followed by intragranular white precipitates. Buytoz et al. [29] demonstrated that in Fe-Cr-C alloy cladding, austenite was the primary solidification phase; as the temperature decreased further, primary austenite rejected C and Cr into the remaining liquid. Since grain boundaries are typically the last regions to solidify, they tend to accumulate higher carbide contents. Consequently, carbides frequently generate at the grain boundaries [30]. Additionally, carbide formation is strongly dependent on Cr content, as Cr acts as a potent nucleation promoter for carbides, whereas Fe exhibits significantly weaker promoting effects on carbide nucleation [31]. The spatial distribution of Cr effectively indicated the carbide

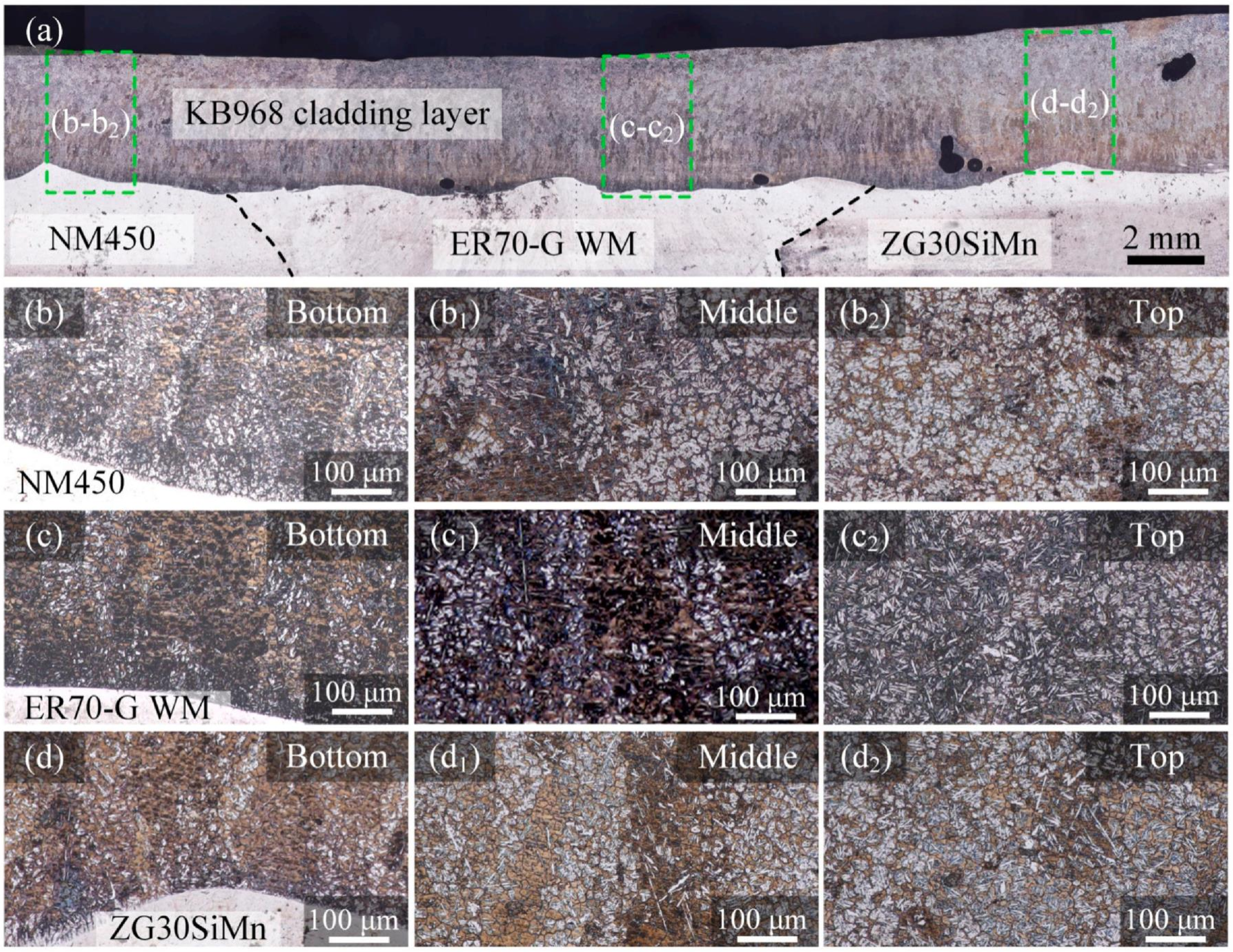

Fig. 4. Optical micrographs of the longitudinal section of the high-dilution-ratio cladding layer: (a) Macroscopic overview, (b–b_2) Across different height zones in the NM450 region (b: bottom, b_1: middle, b_2: top), (c–c_2) Corresponding zones in the ER70-G region, (d–d_2) Corresponding zones in the ZG30SiMn region.

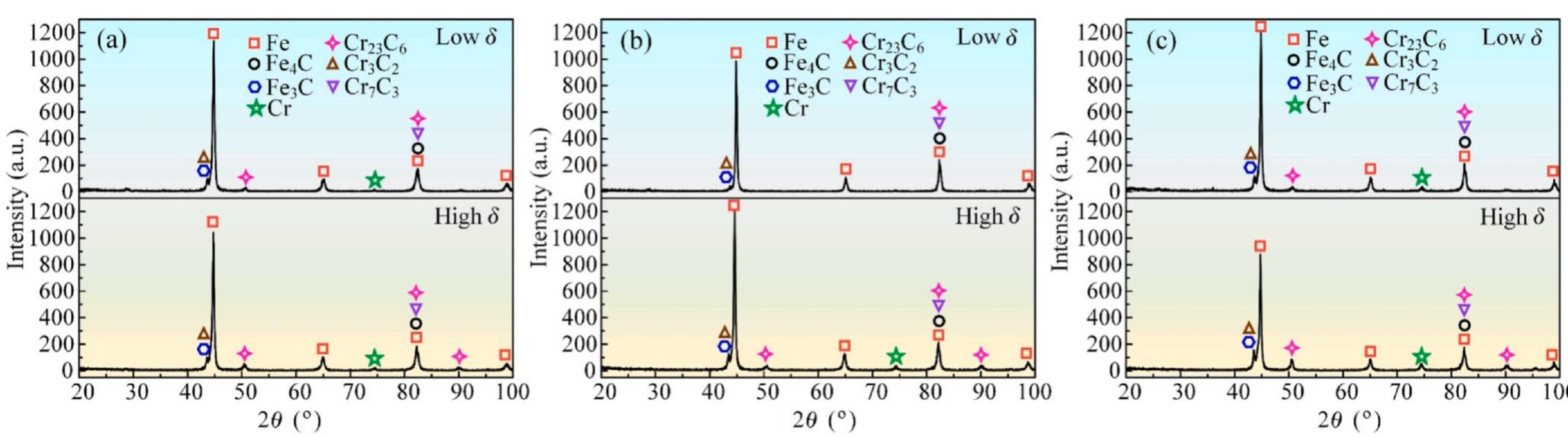

Fig. 5. XRD analysis results of different regions under low and high dilution ratios: (a) In the NM450 regions, (b) In the ER70-G regions, (c) In the ZG30SiMn regions.

distribution, and the white precipitates (at grain boundaries and inside the grains) with high Cr concentrations were highly likely to be carbides. Chuang et al. [26] demonstrated that $M_{23}C_6$ carbides nucleated and grew through a peritectic reaction between the residual liquid and M_7C_3 carbides. These $M_{23}C_6$ carbides were observed to form at the periphery of the M_7C_3 carbides [24], and further analysis revealed that they exhibited a lower Cr content compared to M_7C_3 carbides [9,25]. Based on XRD and SEM results, combined with previous literature findings, the intergranular carbides were identified as Cr_7C_3, whereas the intragranular carbides were determined to be $Cr_{23}C_6$. In contrast, the dark gray intragranular phases with lower Cr concentrations were attributed to (Fe, Cr) solid solutions. With increasing distance from the interface, the proportion of intragranular $Cr_{23}C_6$ carbides gradually decreased. Near the top of the cladding layer, almost no intragranular carbides were observed, with carbides predominantly distributed along grain boundaries (Fig. 7b, c). Given that the top region exhibited the lowest degree of element mixing with the base material, the reduced carbide content here cannot be attributed to insufficient Cr and C. Since the top region of the cladding layer was directly heated by the arc and solidified last, its cooling rate was significantly slower compared to the middle and bottom regions. The slower cooling facilitated the diffusion of Cr and C elements toward grain boundaries, reducing their solid solubility within the grains. As a result, carbide precipitation within the grains was notably diminished.

However, the microstructural distribution underwent significant variations under higher dilution ratios. At this high-dilution condition, the grain boundary phase retained the highest Cr content (> 30 wt.%). Significant intragranular $Cr_{23}C_6$ carbide precipitation was observed

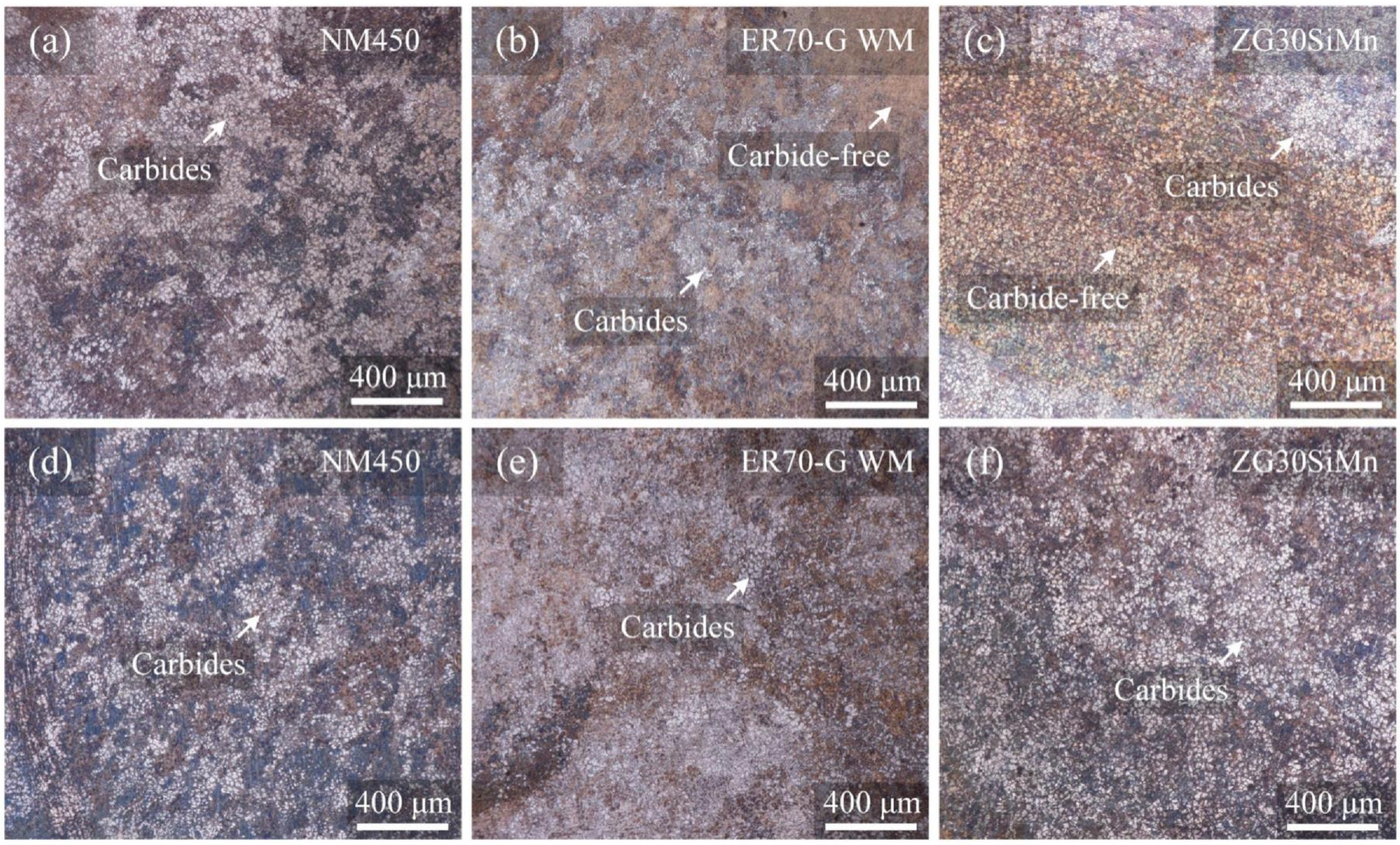

Fig. 6. Optical micrographs of the upper surface: (a–c) Correspond to the NM450, ER70-G, and ZG30SiMn regions under low dilution ratios, (d–f) Correspond to the NM450, ER70-G, and ZG30SiMn regions under high dilution ratios.

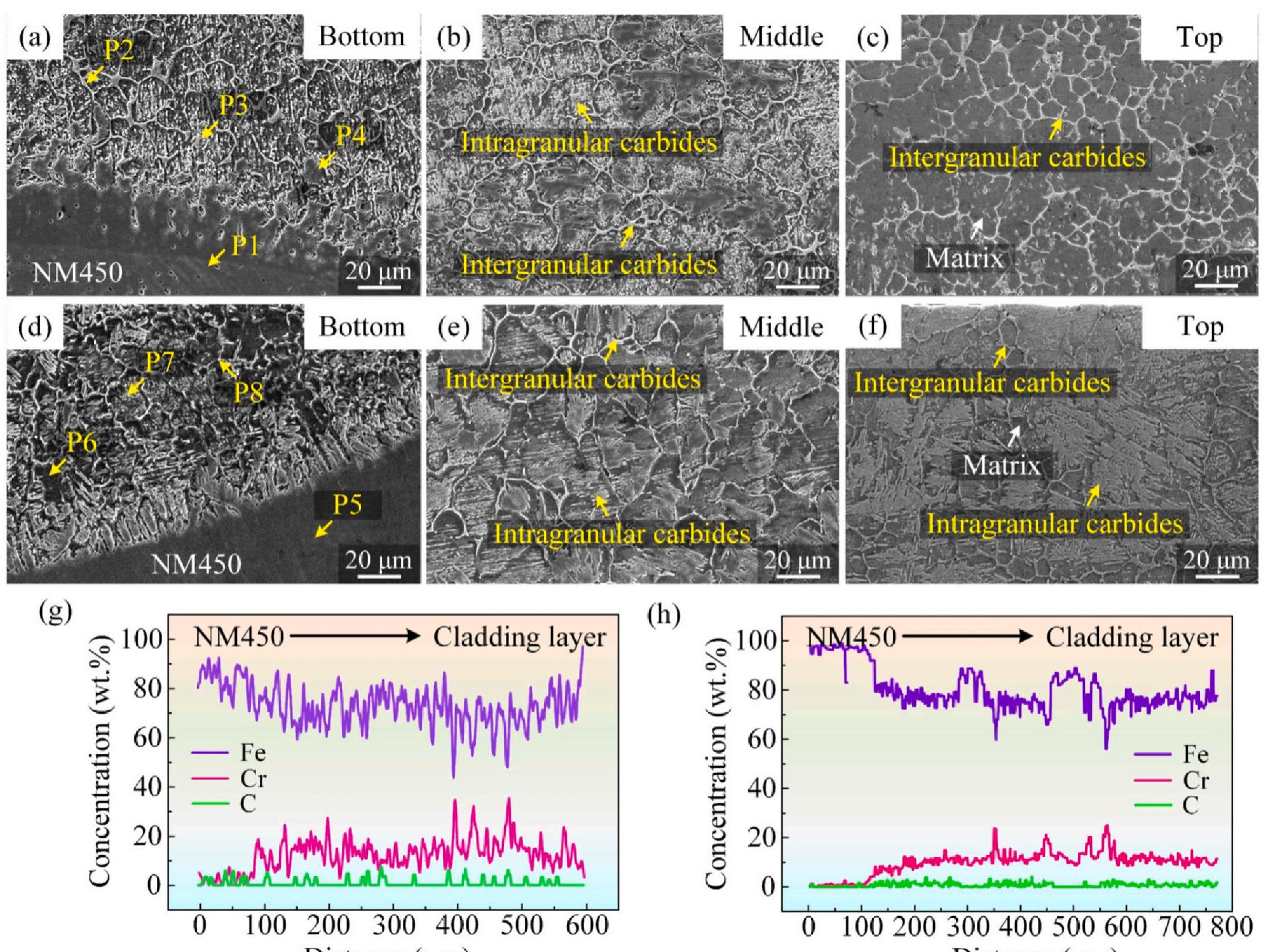

Fig. 7. Microstructures at the NM450/cladding layer interface: (a–c) In the bottom, middle, and top regions at low dilution ratios, (d–f) In the bottom, middle, and top regions at high dilution ratios, (g, h) EDS line scan results at low and high dilution ratios, respectively.

Table 3
EDS point analysis results at the NM450/cladding layer interface (wt.%).

Position	Fe	Cr	Nb	Si	Mn	C
P1	88.4	5.1	2.6	1.0	1.7	1.2
P2	64.4	29.6	0.3	1.2	1.7	2.8
P3	77.9	15.3	0.8	2.2	1.6	2.2
P4	83.4	10.5	0.7	1.5	2.6	1.3
P5	92.6	2.7	0.7	0.5	2.5	1.0
P6	93.4	6.5	—	—	—	0.1
P7	80.1	14.5	0.5	2.1	1.3	1.5
P8	60.6	32.5	0.3	1.6	2.3	2.7

near the top of the cladding layer (Fig. 7f), showing a clear distinction with the low-dilution case. For the high-dilution sample, the heat input was higher and the peak temperature of the molten pool was expected to rise, thereby enhancing the solid solubility of Cr and C elements within the melt. Although elevated temperatures generally promoted the diffusion of Cr and C, the prolonged high-temperature duration simultaneously facilitated grain growth. This extended thermal exposure effectively increased the diffusion distance of Cr and C to grain boundaries, ultimately leading to a higher incidence of intragranular $Cr_{23}C_6$ carbide precipitation and a more uniform distribution of the carbides. The observation aligns with the previous XRD results, indicating an increase in the diffracted intensity of $Cr_{23}C_6$. Fig. 7g, h present EDS line scan results across the NM450/cladding layer interface at low and high dilution ratios, respectively. The more gradual elemental distribution profile of the high-dilution sample confirmed more uniform element mixing under this condition.

Fig. 8 presents the microstructural morphology at the interface between the ER70-G and the cladding layer, exhibiting distinct characteristics compared to the NM450 region. Although the phase distribution remained largely unchanged, with the white precipitates demonstrating higher Cr content than the gray phase (EDS results listed in Table 4), the quantity of carbides was visibly lower than that of the NM450 region. This phenomenon was particularly pronounced in the middle and top zones of the cladding layer, where intragranular carbides were notably scarce, as illustrated in Fig. 8b, c. This discrepancy can be attributed to the base metal's inherent alloy composition. The NM450 base material naturally contains higher levels of Cr and C, which facilitate carbide formation. In contrast, the ER70-G possesses fewer alloying elements. Upon mixing with the cladding filler wire, the Cr and C concentrations were significantly diluted, thereby reducing carbide precipitation. However, when the dilution ratio was increased, the elevated peak temperature and prolonged high-temperature duration substantially enhanced the solid solubility of Cr and C. Concurrently, grain growth (longer diffusion distance for Cr and C) impeded effective grain boundary segregation, promoting extensive intragranular carbide precipitation and diminishing the characteristic carbide network along grain boundaries (Fig. 8c–e). This phenomenon contributed to more uniform carbide distribution, as further corroborated by EDS line-scan analysis (Fig. 8g, h), which revealed smoother elemental distribution profiles with reduced fluctuations under high-dilution condition.

Fig. 9 presents the interfacial microstructure between ZG30SiMn and the cladding layer, with the corresponding EDS results listed in Table 5. Although the Cr content in the ZG30SiMn base material is lower than that in NM450, it is slightly higher than that in ER70-G. Additionally, its carbon content is marginally elevated. Consequently, while the number of intragranular carbides in the ZG30SiMn region was relatively low, a significant amount of dark gray (Fe, Cr) solid solution was observed, as shown in Fig. 9a–c. Under high-dilution condition, the higher heat input promoted the formation of intragranular carbides, exhibiting a trend consistent with the microstructural distribution observed in the NM450

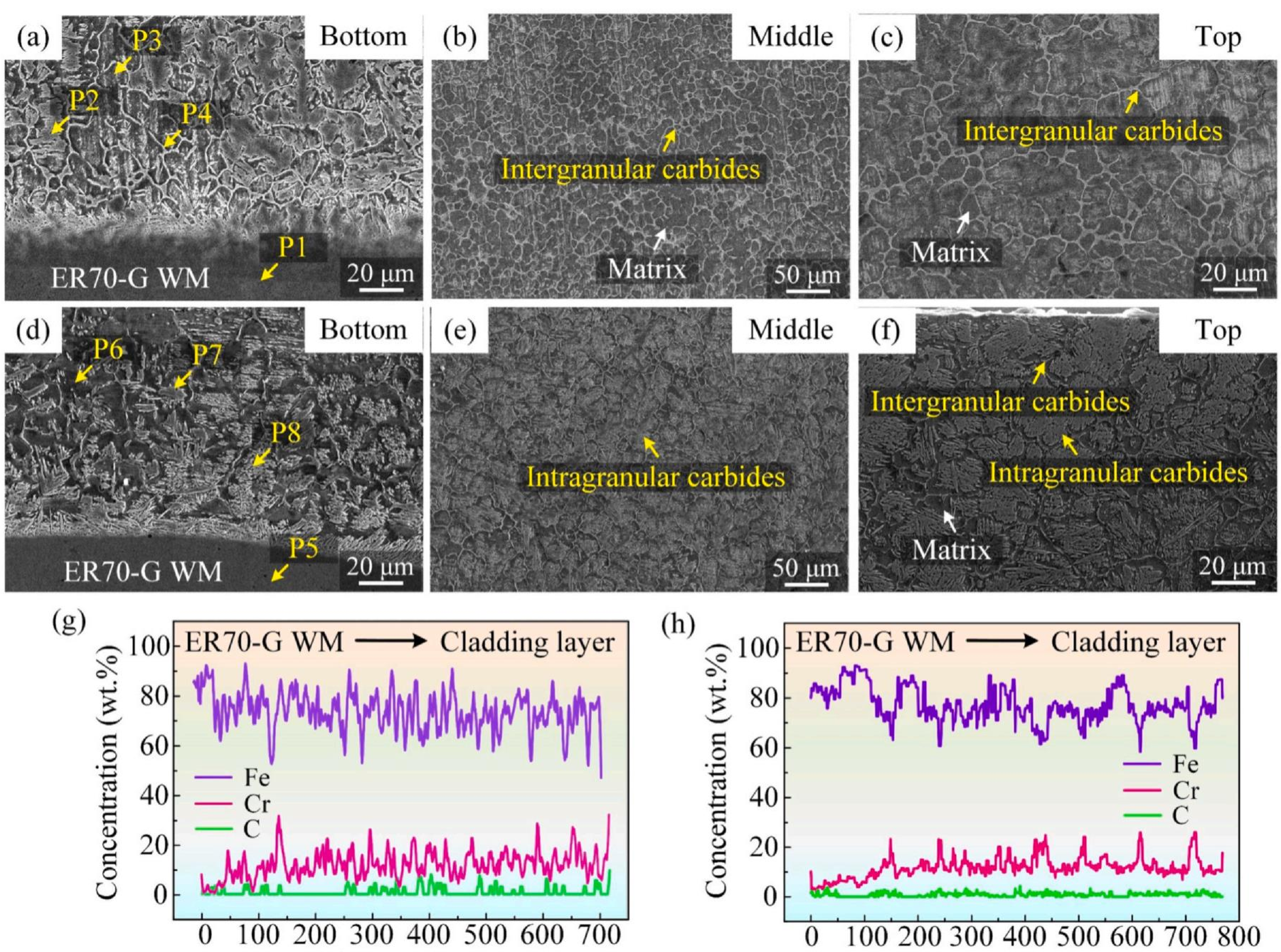

Fig. 8. Microstructures at the ER70-G/cladding layer interface: (a–c) In the bottom, middle, and top regions at low dilution ratios, (d–f) In the bottom, middle, and top regions at high dilution ratios, (g, h) EDS line scan results at low and high dilution ratios, respectively.

Table 4
EDS point analysis results at the ER70-G/cladding layer interface (wt.%).

Position	Fe	Cr	Nb	Si	Mn	C
P1	89.5	4.3	0.4	0.9	3.0	1.9
P2	80.9	13.9	0.5	1.3	1.5	1.9
P3	82.3	11.6	0.2	1.1	2.0	2.8
P4	66.3	26.1	0.3	1.7	3.1	2.5
P5	94.2	1.0	0.1	0.5	2.4	1.8
P6	82.1	12.9	0.3	1.6	1.3	1.8
P7	55.9	38.1	0.5	1.4	1.6	2.5
P8	80.8	14.0	—	1.9	1.7	1.6

Table 5
EDS point analysis results at the ZG30SiMn/cladding layer interface (wt.%).

Position	Fe	Cr	Nb	Si	Mn	C
P1	87.6	8.2	0.2	1.0	1.7	1.3
P2	82.7	11.6	0.1	1.1	2.7	1.8
P3	62.5	30.1	0.7	1.4	2.3	3.3
P4	83.4	12.9	0.2	1.3	1.4	0.8
P5	92.2	3.5	0.2	1.0	1.6	1.5
P6	58.3	34.9	0.4	1.3	1.8	3.3
P7	82.5	12.7	0.1	2.2	0.7	1.8
P8	81.1	11.8	0.4	2.0	2.3	2.4

and ER70-G regions. This suggests that high-dilution sample possessed increased carbide nucleation and precipitation, and improved spatial uniformity, as evidenced by the line-scan results in Fig. 9g, h.

In addition to the microstructures at the binary interfaces, particular attention should be paid to the microstructural characteristics of the ternary mixing zones in both NM450/ER70-G/cladding and ER70-G/ZG30SiMn/cladding systems, as shown in Figs. 10 and 11, respectively. Under the high-dilution condition, a distinct transition in carbide distribution was observed: the continuity of grain boundary carbides was disrupted, while numerous intragranular carbides formed instead, leading to an increased areal fraction of carbide distribution. Notably, in the ER70-G/ZG30SiMn/cladding mixing zone at the low-dilution condition, a carbide-depleted region was clearly visible within the grains (Fig. 11a), indicating poor uniformity of carbide distribution. However, for the high-dilution sample, this carbide-depleted zone disappeared completely, accompanied by a remarkable improvement in the uniformity of carbide distribution.

3.4. Microhardness and wear tests

Hardness measurements were conducted on the cladding layers, with the distribution profiles presented in Fig. 12. Fig. 12a displays the hardness distribution in the NM450 region under varying dilution ratios. The NM450 base material itself exhibited high hardness values ranging between 400 and 450 HV0.2. The hardness of the cladding layer slightly exceeded that of the NM450 base material, measuring 450–500 HV0.2. Notably, when the dilution ratio was increased, the cladding hardness rises significantly, reaching a maximum value of approximately 550 HV0.2. Fig. 12b, c illustrates the hardness profiles for the ER70-G and ZG30SiMn regions, respectively. The base materials of ER70-G and ZG30SiMn showed markedly lower hardness (300 HV0.2) compared to NM450. However, the higher dilution ratio promoted the diffusion of alloying elements from the cladding into the base materials, resulting in elevated hardness near the interfacial region relative to the low-dilution condition. Generally, the cladding layers produced at high dilution ratio

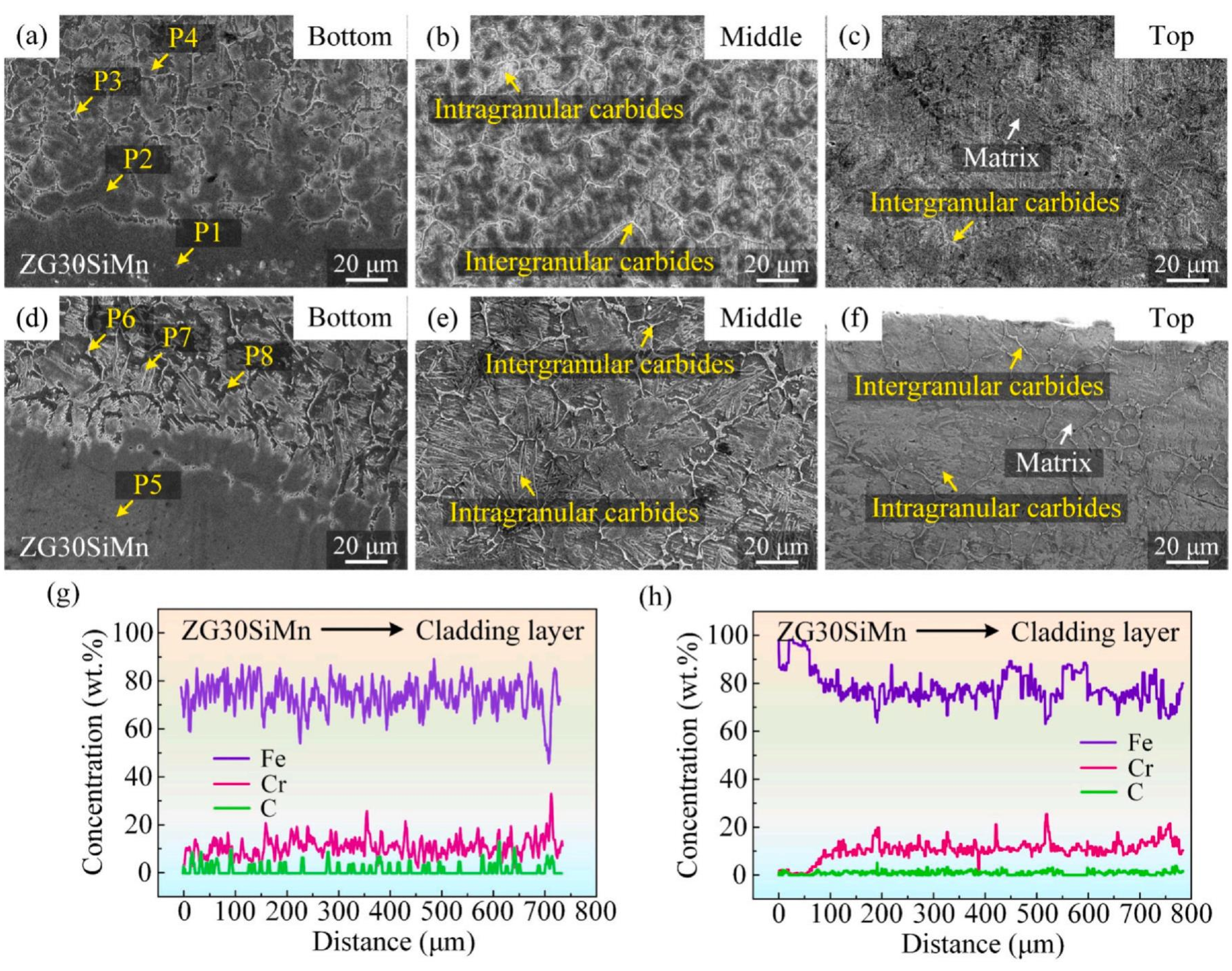

Fig. 9. Microstructures at the ZG30SiMn/cladding layer interface: (a–c) In the bottom, middle, and top regions at low dilution ratios, (d–f) In the bottom, middle, and top regions at high dilution ratios, (g, h) EDS line scan results at low and high dilution ratios, respectively.

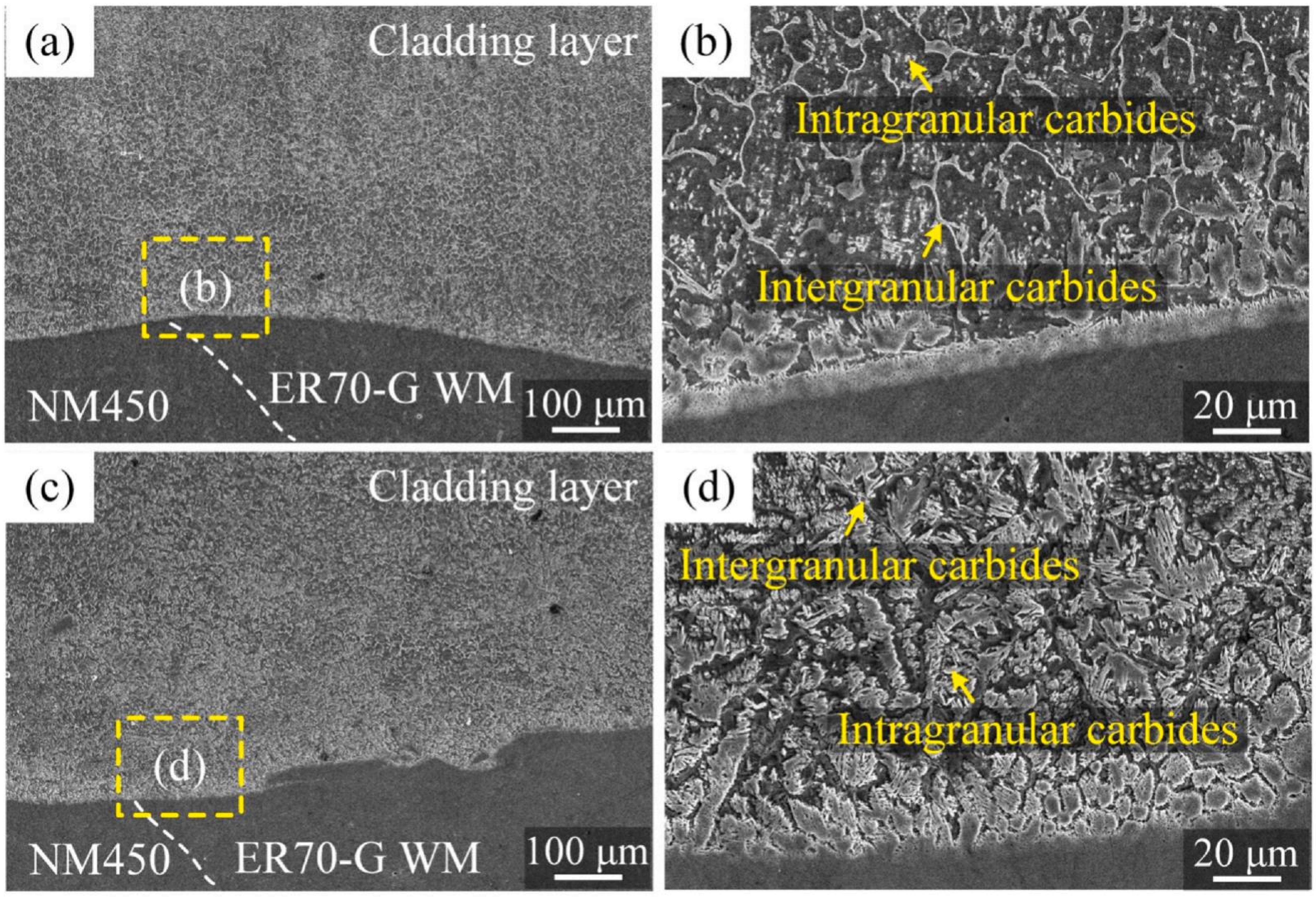

Fig. 10. Microstructures at the compositional mixing zone of NM450/ER70-G/cladding layer: (a, b) At low dilution ratios, (c, d) At high dilution ratios.

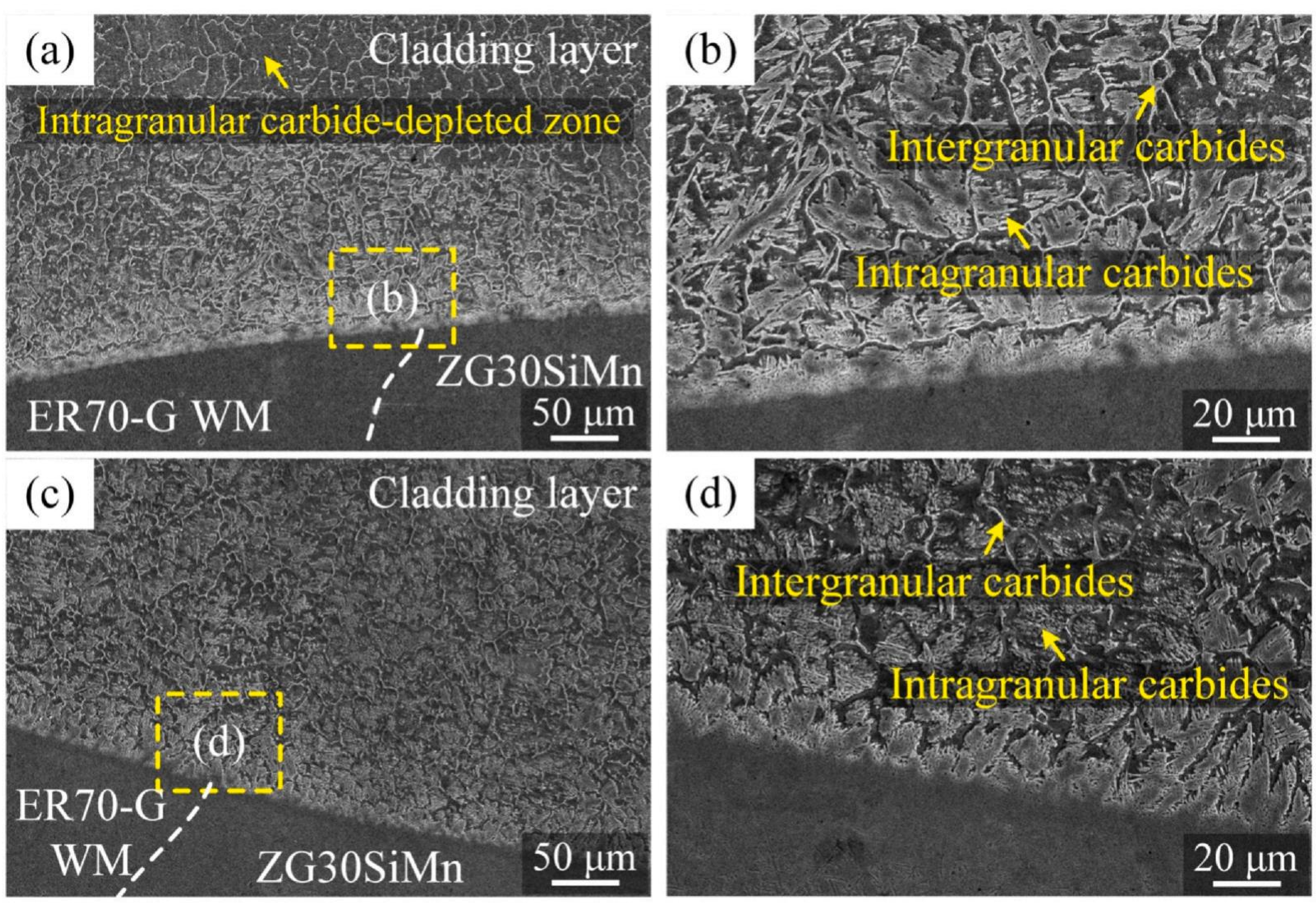

Fig. 11. Microstructures at the compositional mixing zone of ER70-G/ZG30SiMn/cladding layer: (a, b) At low dilution ratios, (c, d) At high dilution ratios.

demonstrated superior hardness, which was attributed to enhanced carbide formation under higher heat input conditions.

The worn surface morphologies are presented in Fig. 13, along with measurements of the wear scar widths. For comparative analysis, the wear properties of the NM450, ER70-G, and ZG30SiMn base materials were also evaluated, as shown in Fig. 13a–c. The wear scar width on the NM450 surface (806.2 μm) was narrower than that of ER70-G (828.9 μm) and ZG30SiMn (831.4 μm), proving the superior wear resistance of the NM450 plate. All three base materials exhibited prominent sliding grooves and adhesion features, indicating a mixed wear mechanism involving both sliding wear and adhesive wear. After cladding with KB968 welding wire, the characteristic sliding grooves disappeared, and adhesive wear played a dominant role. For the NM450 and ER70-G regions, the wear scar widths at high dilution ratio (565.5 μm and 607.8 μm, respectively) were slightly larger than those at low dilution ratio (551.5 μm and 597.5 μm). However, the low-dilution samples exhibited more severe adhesive wear behavior, characterized by large-scale surface spalling. In contrast, the ZG30SiMn region showed a significantly narrower wear scar at high-dilution condition (444.2 μm) compared to the low-dilution sample (599.1 μm), as illustrated in Fig. 13c_1, c_2. The friction coefficient was further measured, as shown in Fig. 14. The friction coefficients of the NM450 and ER70-G regions were close under different

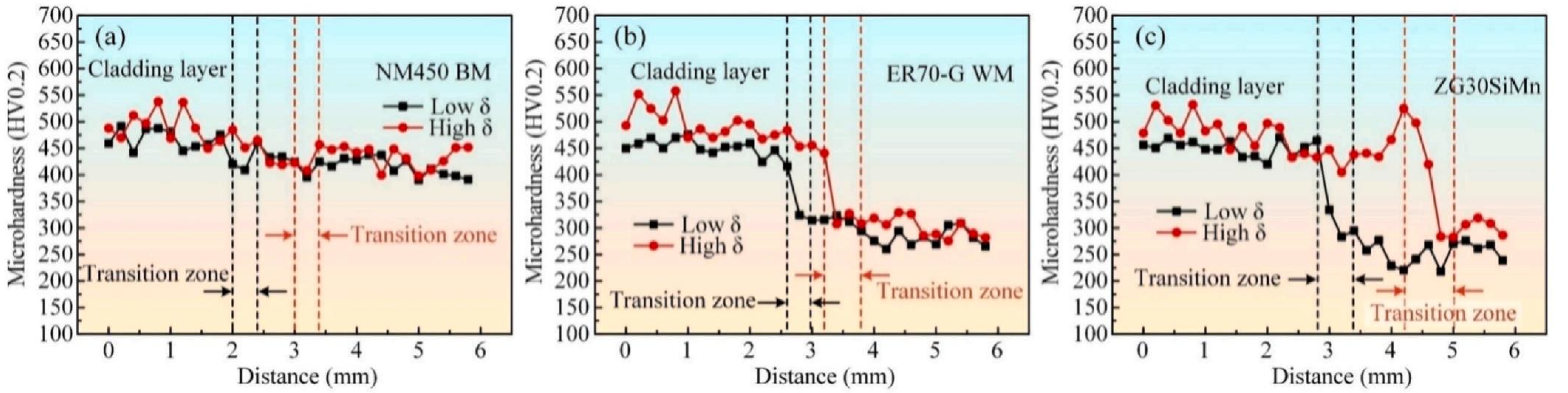

Fig. 12. Microhardness distribution: (a) In the NM450 region, (b) In the ER70-G region, (c) In the ZG30SiMn region.

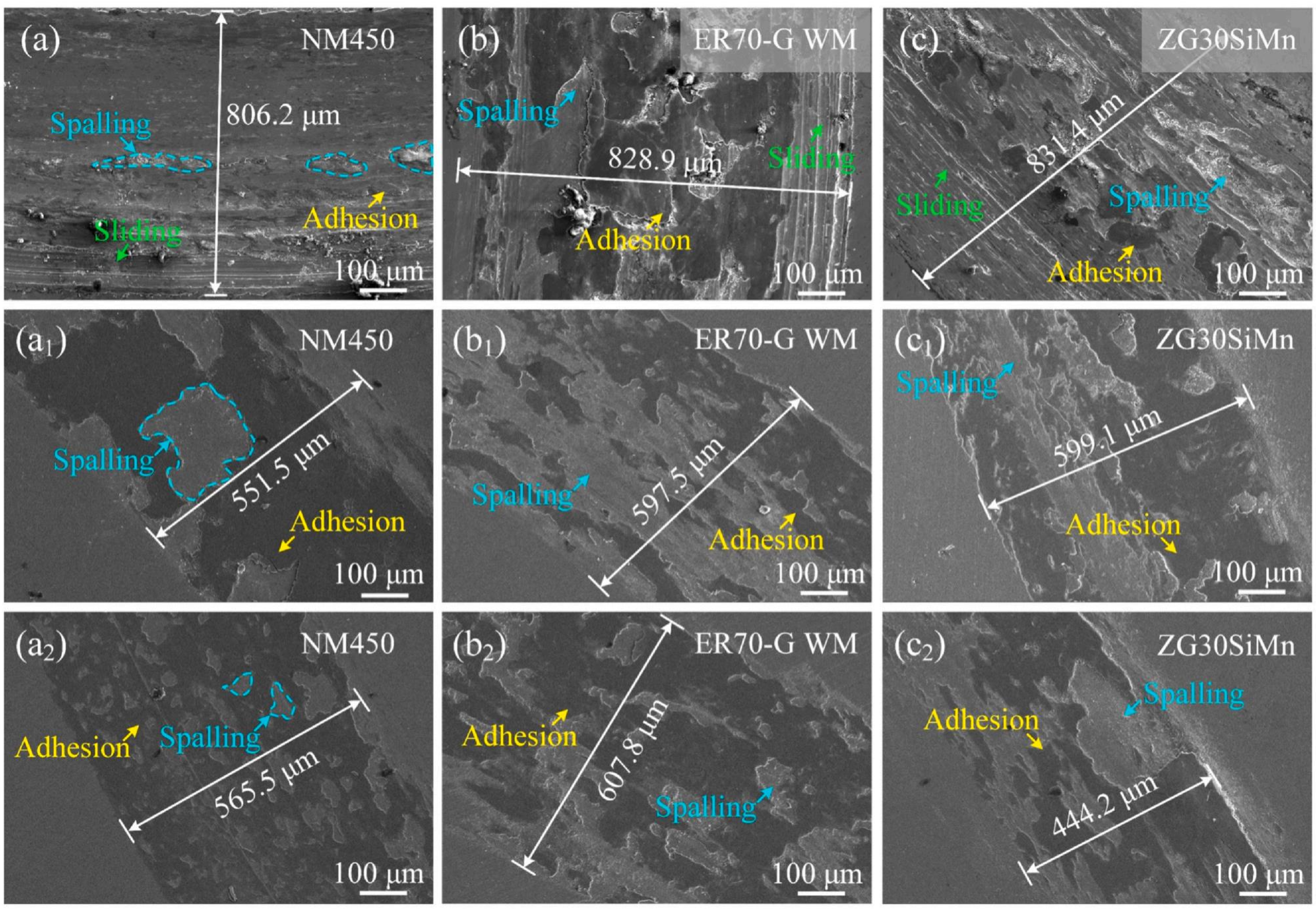

Fig. 13. Worn surface morphologies of base materials and their cladding layers under different dilution ratios: (a–c) NM450, ER70-G substrate, and ZG30SiMn base materials, (a_1–a_2) Cladding layer in the NM450 region under low and high dilution ratios, (b_1–b_2) Cladding layer in the ER70-G region under low and high dilution ratios, (c_1–c_2) Cladding layer in the ZG30SiMn region under low and high dilution ratios.

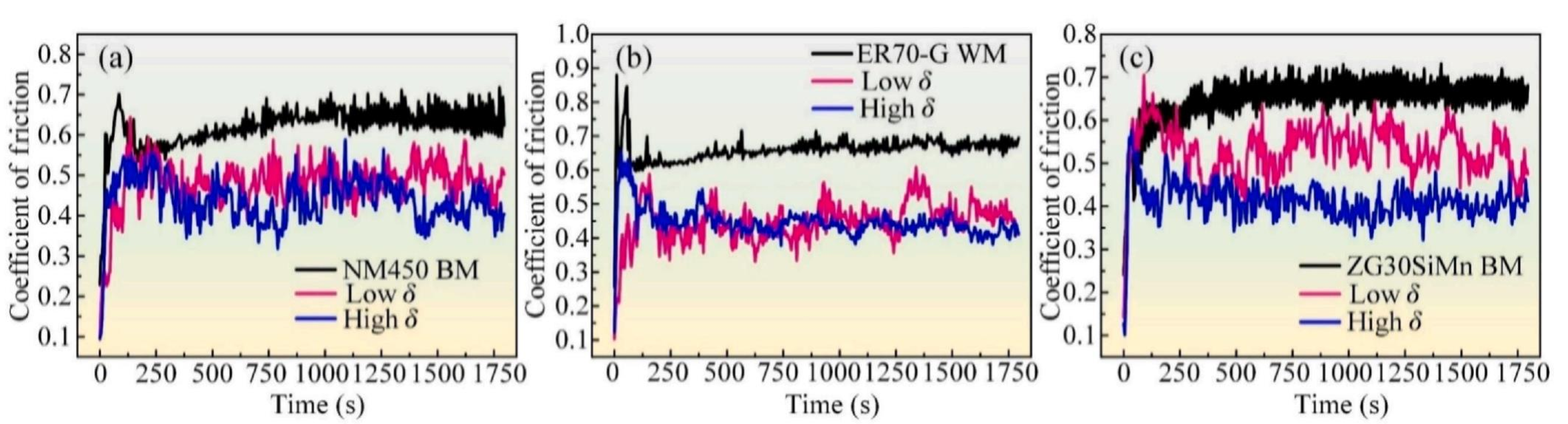

Fig. 14. Coefficient of friction: (a) In the NM450 region, (b) In the ER70-G region, (c) In the ZG30SiMn region.

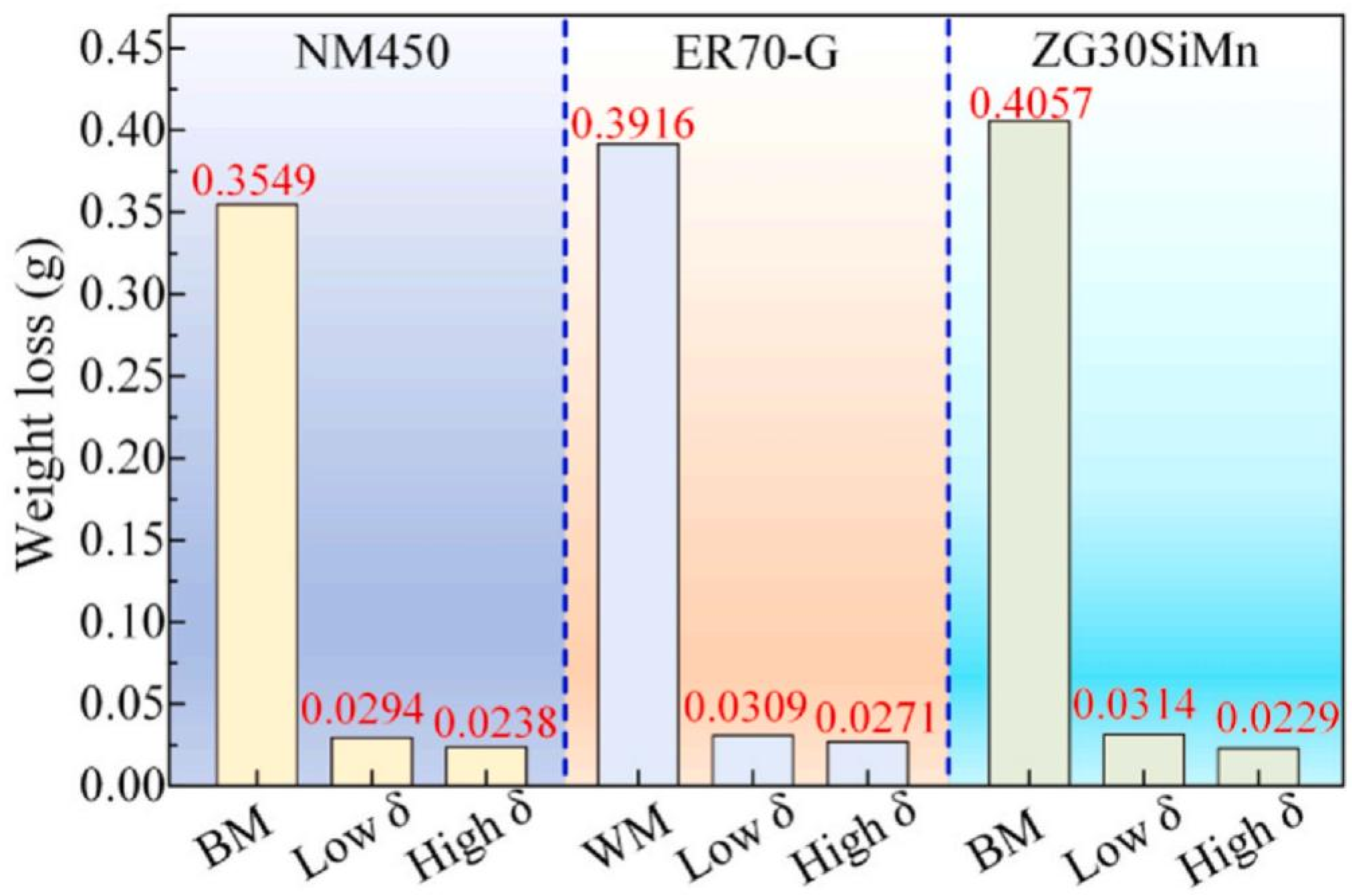

Fig. 15. Wear weight loss comparison under different dilution ratios.

dilution ratios, but slightly lower at high-dilution condition. The ZG30SiMn region, however, demonstrated a significantly lower friction coefficient at high-dilution condition. Notably, all cladding layers exhibited a markedly lower friction coefficient than the base materials. The friction coefficient reflects the resistance encountered during sliding contact under load. A higher friction coefficient means larger resistance and increases surface spalling and damage, whereas a lower value indicates improved wear resistance [30,32]. This verified that the employment of KB968 welding wire improved the overall wear properties of the NM450/ER70-G/ZG30SiMn welded joints, with higher dilution ratio showed better wear resistance. To further precisely assess wear resistance, weight loss was measured and the results are presented in Fig. 15. The results indicated that the NM450, ER70-G, and ZG30SiMn base materials exhibited severe weight loss, with values of 0.3549 g, 0.3916 g, and 0.4057 g, respectively. After cladding treatment, the weight loss was substantially reduced. Moreover, the results confirmed that across all material interfaces (NM450, ER70-G, and ZG30SiMn), samples with high dilution ratio exhibited less weight loss than those processed at low-dilution condition. Combined analysis of worn surface morphology, coefficient of friction, and weight loss demonstrates that the high-dilution sample yields superior tribological performance compared to the low-dilution one.

The wear performance of materials is closely related to the quantity, size, and distribution of wear-resistant phases. Conventionally, a lower dilution ratio is believed to help preserve alloying elements (such as Cr and C) in the cladding layer, thereby promoting the formation of hard wear-resistant phases and reducing friction-induced damage [8,28,33]. However, in this study, the high-dilution samples demonstrated superior wear resistance. This can be attributed to the fact that a moderate increase in current (and thus heat input) prolongs the metallurgical reaction time at elevated temperatures and enhances elemental diffusion. These effects not only increase the precipitation of carbides but also improve their distribution uniformity, ultimately leading to enhanced wear resistance. In addition, the high-efficiency arc wire cladding technology yields a thicker cladding layer compared to the powder cladding method. Although significant dilution or elemental mixing occurs at the interface regions, the top zones of thick cladding layer are less affected by the degree of dilution.

4. Conclusions

This study employed Fe-Cr-C welding wire to fabricate cladding layers on NM450/ER70-G/ZG30SiMn dissimilar steel welded joints, and investigated the microstructure distribution and wear resistance under different dilution ratios. Key findings are summarized as follows:

(1) The cladding layers exhibited a crack-free morphology across all three heterogeneous interfaces (NM450/cladding, ER70-G/cladding, and ZG30SiMn/cladding). Additionally, higher heat input led to an increased dilution ratio between the cladding layer and base material.
(2) Cr_7C_3 carbides were observed to precipitate along grain boundaries, whereas $Cr_{23}C_6$ carbides tended to form within grains. Compared to the low-dilution condition, the high-dilution sample exhibited enhanced precipitation of $Cr_{23}C_6$ carbides with a more homogeneous distribution.
(3) The NM450/ER70-G/ZG30SiMn heterogeneous welded joints showed improved wear performance after cladding treatment, with the high-dilution sample presenting superior wear resistance. Despite severe elemental mixing at the interface, the top region of the cladding layer was minimally affected by dilution-related adverse effects.

Future research could explore surface cladding experiments on dissimilar joints such as NM450/ER70-G/ZG30SiMn across a broader range of process parameters to establish more comprehensive experimental guidelines. Additionally, wear performance under varying friction loads should be investigated, as the current study encountered difficulties in extracting 3D topographical data of worn surfaces, likely due to shallow wear scars resulting from relatively low applied loads.

CRediT authorship contribution statement

Ning Xiao: Writing – original draft, Writing – review & editing. **Yujie Tao:** Formal analysis, Methodology. **Yiheng Liu:** Data curation, Software. **Haoyu Kong:** Data curation, Visualization. **Qingjie Sun:** Resources, Supervision. **Ninshu Ma:** Conceptualization, Supervision.

Declaration of Competing Interest

The authors declare the following financial interests/personal relationships which may be considered as potential competing interests: Ninshu Ma is an Editorial Board Member for China Welding and was not involved in the editorial review or the decision to publish this article. Ning Xiao reports a relationship with METALLECO Inc that includes: employment. Yujie Tao reports a relationship with STUAA Automation Co., Ltd. that includes: employment. Yiheng Liu reports a relationship with STUAA Automation Co., Ltd. that includes: employment. Haoyu Kong reports a relationship with STUAA Automation Co., Ltd. that includes: employment. Qingjie Sun reports a relationship with METALLECO Inc that includes: employment. The other authors declare that they have no competing interests.

Acknowledgements

This research did not receive any specific grant from funding agencies in the public, commercial, or not-for-profit sectors.

References

[1] Liu T, Wu Q, Fang Y, Wang Y, Chu Q, Chen Y, et al. Characterization of fusion boundary between low alloy steel and stainless steel cladding. J Mater Res Technol 2024;28:2363–78.
[2] Yun X, Wang J, Zhu Q, Chen Z, He B. Microstructure and wear resistance of Fe-based and Co-based coating of AISI H13. China Weld 2019;28(3):54–60.
[3] Aslam M, Kumar Chandan G, Kumar Kanchan B. Hard and wear resistant AISI304 stainless steel clad layer deposited on mild steel substrate by TIG cladding. Manuf Lett 2024;42:34–9.
[4] Wang Y, Yu T, Zhang Y, Sun J, Sun Z. Process parameter optimization of Fe-based coating on ductile iron using laser cladding with grey related analysis. Opt Laser Technol 2025;181:11906–111915.
[5] Zhang Y, Zhan H, Wan Q, Wang R, Zhang X, Wang W. Multi-objective optimization of process parameters for rectangular laser cladding of Fe-based alloy wear-resistant coatings. Surf Coat Technol 2025;503:131990–2004.
[6] Liu Z, Han C, Cao X, Guo J, Li H, Lin Y, et al. Microstructure and wear behavior of AISI 316L austenitic stainless steel coating fabricated by laser cladding and plasma nitriding. Mater Lett 2025;383:137951–5.
[7] Santana DA, Koga GY, Wolf W, Bataev IA, Ruktuev AA, Bolfarini C, et al. Wear-resistant boride reinforced steel coatings produced by non-vacuum electron beam

cladding. Surf Coat Technol 2020;386:125466–76.

[8] Durmuş H, Çömez N, Gül C, Yurddaşkal M, Yurddaşkal M. Wear performance of Fe-Cr-C-B hardfacing coatings: dry sand/rubber wheel test and ball-on-disc test. Int J Refract Met Hard Mater 2018;77:37–43.

[9] Yüksel N, Şahin S. Wear behavior - hardness - microstructure relation of Fe-Cr-C and Fe-Cr-C-B based hardfacing alloys. Mater Des 2014;58:491–8.

[10] Ding T, Li C, Jing W, Di X, Hu W. Influences of boron on the microstructural characteristics and wear performance of hypereutectic Fe-Cr-C-Mo-*x*B hardfacing alloy. Surf Coat Technol 2024;478:130415–26.

[11] Li G, Dong H, Zhang C, Li Y, Wang Y. Achieving wear resistance enhancement of Fe-Cr-B-C alloy coating by laser cladding and remelting processes. Opt Laser Technol 2025;190:113291–301.

[12] Long W, Sun H, Liu D, Qin J, Zhang L, Lu H. Effect of TiC addition on the microstructure and wear resistance of induction brazed nickel-based coating in air. China Weld 2022;31(4):1–6.

[13] Gou J, Chen K, Le M, Wang G, Liu J, Tan G, et al. A study on the scratch behavior and two-body abrasion wear resistance of TiC-modified E690 steel cladding. Wear 2025;570:205923–33.

[14] Mo K, Cao L, Zhao D, Long Y, Zhong J, Zhong J, et al. Study on the microstructure and wear resistance of laser clad martensitic stainless steel 420 with different content of TiC. Mater Today Commun 2025;46:112615–28.

[15] Huang D, Tong Y, Hua M, Mou H, Liu J, Cai Z, et al. Ultra wear resistant TiC-Fe coating prepared by high efficient and economic plasma cladding method. China Weld 2024;33(1):20–6.

[16] Wang X, Zhang Z, Men Y, Li X, Liang Y, Ren L. Fabrication of nano-TiC functional gradient wear-resistant composite coating on 40Cr gear steel using laser cladding under starved lubrication conditions. Opt Laser Technol 2020;126:106136–44.

[17] Aslam M, Sahoo CK. Development of hard and wear-resistant SiC-AISI304 stainless steel clad layer on low carbon steel by GMAW process. Mater Today Commun 2023;36:106444–55.

[18] Qin J, Yang J, Liu P, Liu D, Lu H, Liao Q, et al. Microstructure and properties of induction brazing nickel base/WC composite coating. China Weld 2023;32(1):27–34.

[19] Ding H, Cui T, Wang W, Lin Q, Wang L, Yang Y, et al. Laser cladding WC/Fe composite coating on nose rail of turnout: microstructure characteristics and wear behaviors. Wear 2025;570:205929–42.

[20] Wei R, Mao M, Liang J, Zhao C, Ouyang C, Wang R, et al. Study of the effect of overlap rate on the failure form, microstructure and wear resistance of multilayer laser cladding on grey cast iron surfaces. Tribol Int 2024;194:109568–84.

[21] Liu X, Chen Z, Liu Y, Dong W, Tang H, Li H, et al. Enhanced wear resistance of laser cladding Al0.5CoCrFeNi coating via in-situ reaction synthesis between Ti and B4C particles. J Alloy Compd 2025;1031:180965–77.

[22] Shayanfar P, Daneshmanesh H, Janghorban K. Parameters optimization for laser cladding of Inconel 625 on ASTM A592 steel. J Mater Res Technol 2020;9:8258–65.

[23] Sadeghi F, Najafi H, Abbasi A. The effect of Ta substitution for Nb on the microstructure and wear resistance of an Fe-Cr-C hardfacing alloy. Surf Coat Technol 2017;324:85–91.

[24] Tang X, Chung R, Pang C, Li D, Hinckley B, Dolman K. Microstructure of high (45 wt %) chromium cast irons and their resistances to wear and corrosion. Wear 2011;271:1426–31.

[25] Lin C, Lai H, Kuo J, Wu W. Effect of carbon content on solidification behaviors and morphological characteristics of the constituent phases in Cr-Fe-C alloys. Mater Charact 2011;62:1124–33.

[26] Chung R, Tang X, Li D, Hinckley B, Dolman K. Microstructure refinement of hypereutectic high Cr cast irons using hard carbide-forming elements for improved wear resistance. Wear 2013;301:695–706.

[27] Sousa J, Gil G, Barbosa M, Garcia D, Lobato M, Machado P. Tribological performance under abrasive wear of Fe-Cr-C + Nb coating deposited by FCAW process. Wear 2023;523:204824–36.

[28] Sá de Sousa J, Lobato M, Garcia D, Machado P. Abrasion resistance of Fe-Cr-C coating deposited by FCAW welding process. Wear 2021;476:203688–99.

[29] Buytoz S. Microstructural properties of M7C3 eutectic carbides in a Fe-Cr-C alloy. Mater Lett 2006;60:605–8.

[30] Mousavi Anijdan S, Sabzi M, Najafi H, Jafari M, Eivani A, Park N, et al. The influence of aluminum on microstructure, mechanical properties and wear performance of Fe-14% Mn-1.05%C manganese steel. J Mater Res Technol 2021;15:4768–80.

[31] Bedolla-Jacuinde A, Hernández B, Metallkunde L. SEM study on the M_7C_3 carbide nucleation during eutectic solidification of high-chromium white irons. Z Met 2005;96:1380–5.

[32] Mahade S, Awe S, Björklund S, Lukáč F, Mušálek R, Joshi S. Sliding wear behavior of a sustainable Fe-based coating and its damage mechanisms. Wear 2022;500–501:204375–88.

[33] Balasubrarnanian V, Lakshminarayanan A, Varahamoorthy R, Babu S. Application of response surface methodology to prediction of dilution in plasma transferred arc hardfacing of stainless steel on carbon steel. J Iron Steel Res Int 2009;16:44–53. https://doi.org/10.1016/S1006-706X(09)60009-1.